International Journal of Heat and Mass Transfer 271 (2026) 129392

Contents lists available at ScienceDirect

International Journal of Heat and Mass Transfer

journal homepage: www.elsevier.com/locate/ijhmt

Scaling law for natural convection heat transfer in supercritical fluids considering the vapor-like-layer effect

Yaqin Liu [a], Jinliang Xu [a,b,*], Yulin Mao [a], Guanglin Liu [a]

[a] Beijing Key Laboratory of Multiphase Flow and Heat Transfer for Low Grade Energy Utilization, North China Electric Power University, Beijing 102206, China
[b] Key Laboratory of Power Station Energy Transfer Conversion and System of Ministry of Education, North China Electric Power University, Beijing 102206, China

ARTICLE INFO

Keywords:
Scaling law
Supercritical fluid
Vapor-like-layer effect
Numerical simulation
Experiment

ABSTRACT

Available experiments on supercritical fluids have shown a vapor-like-layer effect during natural convection heat transfer (NCHT); however, a quantitative description of this effect remains challenging. Here, numerical simulations of NCHT were performed using a horizontal platinum wire heater with a 70-μm diameter and 22.0-mm length, immersed in a large supercritical carbon dioxide (sCO_2) pressure vessel. The results were in good agreement with the experimentally measured values. A physical model consisting of a vapor-like-layer region and a bulk fluid region was proposed to locate the interface between the two regions at the pseudo-critical temperature T_{pc}. Unlike in previous studies, supercritical NCHT was treated via natural convection mechanism in the bulk fluid region, represented by a modified Rayleigh number $\mathbf{Ra_m}$, and with a heat transfer deterioration number **De** to reflect the vapor-like-layer effect. Our simulations, with pressures, heat fluxes, and wall temperatures in the ranges of 8–16 MPa, 112–917 kW/m^2, and 334–672 K, yielded a correlation for Nusselt number **Nu** of the form $\mathbf{Nu} = 1.92 \cdot \mathbf{Ra}_m^{0.22}\mathbf{De}$, thus providing a scaling law of **Nu**~**De**, and a self-similarity characteristic of non-dimensional vapor-like-layer size $\mathbf{R}_\delta^*$. These scaling laws are applicable to sCO_2 heat transfer with other parameter ranges and even for supercritical water. The correlation-predicted **Nu** was in good agreement with the experimental data, even though these data were not involved in the development of the correlation. Thus, our work presents new scaling laws to effectively understand the underlying mechanism and increases the prediction accuracy of supercritical NCHT.

1. Introduction

Natural convection refers to the self-establishment of convective flow due to heating-induced buoyancy force, as opposed to an external force generated by a fan or pump. Natural convection is frequently observed in our daily life and in various applications [1–4]. Subcritical natural convection heat transfer (NCHT) without phase change has been widely investigated by experimental, theoretical, and numerical approaches [2,5–7]. Usually, NCHT is correlated as $\mathbf{Nu} = c_1 \cdot \mathbf{Ra}^{c_2}$, where **Nu** is the Nusselt number; **Ra** is the Rayleigh number; and c_1 and c_2 are experimentally determined coefficients that vary with the heat source size, its inclination angle with respect to gravity, and working fluid [5,6]. Available studies indicate a monotonic increase of **Nu** with **Ra**, i.e., the heat transfer coefficient increases with the heat source temperature or applied heat flux [5–7].

The volume expansion coefficient β is a key parameter influencing the heat transfer coefficient [1]. Assuming that fluid density does not vary with temperature, typically, buoyancy-driven natural convection is suppressed and conduction heat transfer significantly dominates heat transfer. In the supercritical domain, physical properties of fluids change dramatically, especially when a critical or pseudo-critical temperature T_{pc} is exceeded [8]. In the classical NCHT framework, due to significantly varying fluid densities at supercritical pressures, NCHT should be enhanced as wall temperature increases. This logical deduction contradicts experimental observations and numerical simulations at supercritical pressures [9–12]. As the wall temperature or heat flux continuously increases, the heat transfer coefficient increases sharply, reaches a peak value, and then decreases or even attains a constant value [9–12]. This phenomenon can be qualitatively explained by the fact that

Abbreviations: BL, boiling-like; DC, direct-current; EL, evaporation-like; NCHT, natural convection heat transfer; Ni-Cr, nickel-chromium; Pt, platinum; sCO_2, supercritical carbon dioxide; sH_2O, supercritical water; TEB, transition from evaporation-like to boiling-like.

* Corresponding author at: Beijing Key Laboratory of Multiphase Flow and Heat Transfer for Low Grade Energy Utilization, North China Electric Power University, Beijing 102206, China.
E-mail address: xjl@ncepu.edu.cn (J. Xu).

https://doi.org/10.1016/j.ijheatmasstransfer.2026.129392
Received 20 April 2026; Received in revised form 27 July 2026; Accepted 3 August 2026
Available online 8 August 2026
0017-9310/© 2026 Elsevier Ltd. All rights are reserved, including those for text and data mining, AI training, and similar technologies.

Nomenclature

Roman symbols

A	area, m^2
a	thermal diffusivity, m^2/s
c_p	specific heat capacity, J/(kg K)
c_1	coefficient
c_2	coefficient
D_0	diameter of wire, m
D_S	equivalent diameter of vapor-like-layer, m
e	relative error
e_A	the mean relative error, $\sum_{i=1}^{n} e_i/n$
e_R	the mean absolute relative error, $\sum_{i=1}^{n} \lvert e_i \rvert/n$
e_S	the root-mean-square relative error, $\sqrt{\sum_{i=1}^{n} e_i^2/n}$
g	acceleration of gravity, m/s^2
H_3	non-dimensional parameters in instability analysis
h	heat transfer coefficient, $W/(m^2 \cdot K)$
L	length, m
n	node number
P	pressure, MPa
Q	total heating power, W
R	radius , m
R_S	equivalent radius of vapor-like-layer, m
R_S^*	dimensionless equivalent radius of vapor-like-layer
R_a	resistance, Ω
R_h	resistance of heating Pt wire, Ω, $\rho_{Pt}L/A$
R_{NC}	thermal resistance of natural convection region, $(m^2 \cdot K)/W$, $(T_{pc} - T_b)/q_w$
R_{VL}	thermal resistance of vapor-like-layer, $(m^2 \cdot K)/W$, $(T_w - T_{pc})/q_w$
R_t	total resistance, $(m^2 \cdot K)/W$, $(T_w - T_b)/q_w$
S	area, m^2
T	temperature, K or °C
T_r	reference temperature. K, $(T_w + T_b)/2$or $(T_{pc} + T_b)/2$
t	time, s
U	voltage, V
u	velocity, m/s
v	velocity, m/s
w	data or properties of fluid
x	x-axis
y	y-axis

Greek symbols

β	volumetric expansivity, 1/K
ΔT_w	wall superheating, K, $\Delta T_w = T_w - T_{pc}$
$\Delta\theta$	the circumferential angle, °
ε	relative tolerance
λ	thermal conductivity, W/(m·K)
μ	dynamic viscosity, Pa·s
ν	kinematic viscosity, m^2/s
ρ	density, kg/m^3
ρ_{Pt}	electrical resistivity of Pt wire, Ω·m
ϕ_h	volumetric heat source, W/m^3, $U_h^2/(\rho_{Pt}L^2)$

Non-Dimensional Numbers

De	heat transfer deterioration number, $\boldsymbol{\Theta}/\mathbf{R}_S^*$
Nu	Nusselt number, hD_0/λ
Ra	Rayleigh number, $g\beta(T_w - T_b)D_0^3/(\nu a)$
Ra$_m$	modified Rayleigh number, $g\beta(T_{pc} - T_b)D_0^3/(\nu a)$
Θ	dimensionless excess temperature, $(T_w - T_{pc})/(T_w - T_b)$

Subscripts or Superscripts

0	platinum wire
a	safety resistor
b	bulk fluid
exp	experiment
end	final time of simulation
f	fluid
h	platinum wire
i	node
m	modified
NC	natural convection region
pc	pseudo-critical
pre	prediction
r	reference
S	area
sim	simulation
t	total
VL	vapor-like-layer
w	wire.

when temperature exceeds T_{pc}, on the one hand, the fluid density decreases sharply. On the other hand, the thermal conductivity of the fluid also drastically decreases, which adversely affects the heat transfer [9,13,14]. This unconventional trend in heat transfer is balanced by a positive as well as a negative effect. At high heating intensities, the surface of the heat source is covered by a vapor-like layer with a low thermal conductivity; this phenomenon is similar to film-boiling at subcritical pressures [9–11,15–17]. Nevertheless, NCHT at supercritical pressures is still correlated using a form similar to that used at subcritical pressures [15,16], and a quantitative description of the vapor-like-layer effect in supercritical NCHT is not yet available.

Investigations on supercritical NCHT can be dated back to the 1960s. Knap and Sabersky investigated natural convection from a heater wire to carbon dioxide (CO_2) near its critical point [18]. Three flow patterns were observed, including the conventional natural convection flow, a highly turbulent flow with bubble-like pattern, and an oscillating flow with bubble-like pattern. They stated that the bubble-like pattern can occur near the critical point, which is dependent not only on the variations in fluid properties, but also on the geometry of the heating surface [18]. Abadzic and Goldstein measured the heat transfer in CO_2 around a horizontal platinum (Pt) wire near the critical point [15]. Below the critical point, film boiling appeared with rising vapor in columns or sheets, which were similar to those that would appear above the critical point [15]. Hahne and Neumann investigated heat transfer in CO_2 using nickel-alloy and Pt wires as heaters [17]. They observed three flow regimes, namely laminar, oscillatory, and turbulent film flows; they reported only laminar flow with Pt wires with high thermal diffusivity, but all three regimes are observed with nickel-chromium (Ni-Cr) wires with low thermal diffusivity [17].

At subcritical pressures, phase change from liquid to vapor involves both evaporation and boiling modes. The former does not generate new interfaces, while the latter does [1]. He et al. [9] examined whether evaporation-like (EL) and boiling-like (BL) modes would occur at supercritical pressures, using Pt and Ni-Cr wires as heat sources. They identified the EL mode only for the Pt wire; however, for the Ni-Cr wire, the EL mode, a transition mode from EL to BL (TEB mode), and the BL mode were observed. Furthermore, heat transfer was seen to deteriorate in the EL mode. The heat transfer coefficients were higher with the BL mode due to the oscillation flow and disturbance effect caused by a bubble-like structure. They introduced the small-perturbation theory to

propose a new non-dimensional parameter, H_3, to explain the difference between the two heat transfer modes. Table 1 lists some of the natural convection experiments performed near the critical point and in supercritical pressure region [9,10,15,16,19,20].

In summary, the above literature survey suggests that: (1) Available studies focused mostly on near-critical-point region [10,15–21] and additional studies should be performed at pressures significantly higher than the critical pressure; (2) Both film-boiling heat transfer (EL mode) and bubble-like phenomenon (BL mode) were observed [9]. The EL mode is a stable heat transfer mode, with a vapor-like film attached to the heater surface, which deteriorates the heat transfer due to its low thermal conductivity [9]. Alternatively, the bubble-like pattern strongly disturbs the flow field, thereby enhancing the heat transfer [9,17]. However, quantitative descriptions of these effects are scarce in the literature. (3) Under the film-like heat transfer, the boiling curve exhibits a non-monotonic trend of heat transfer coefficients with respect to wall superheating [10], where wall superheating is defined as the wall temperature minus the pseudo-critical temperature at the corresponding pressure [9]. Consequently, there is a strong need to explore the underlying mechanism.

The objective of this study is to develop new dimensionless numbers and scaling laws for natural convection at supercritical pressures. The core idea is to divide the temperature domain into two regions: a vapor-like-layer region and a bulk fluid region. The interface between the two regions is located at the pseudo-critical temperature. The emphasis in the vapor-like-layer region is on heat transfer deterioration, while the emphasis in the bulk fluid region is on natural convection. This research is organized as follows: First, both the experimental and numerical simulation data for supercritical NCHT were collected. Second, based on the collected data, dimensionless numbers and scaling laws were developed. Third, the developed scaling laws were examined for their applicability to other operating conditions and for other fluids, such as supercritical water. The heat transfer coefficients from the developed correlation were compared with the experimentally measured ones from the literature.

2. Data collection for developing new dimensionless numbers and scaling laws

This section presents experiments and numerical simulations conducted to collect data for the development of dimensionless numbers and scaling laws.

2.1. Experimental data

2.1.1. Experimental setup

The experimental data were taken from our previous research [9,22], which also provide details of the experimental techniques employed. Therefore, here, the same is touched upon only briefly. As shown in Fig. 1a, the experimental setup consists of a pressure stabilizer system (1−4), temperature stabilizer system (10, 11), high-pressure vessel (12), heater-wire test Section (5, 8, 13), high-speed camera system (9, 14, 15), and data acquisition system (6, 7). Before starting the experiment, non-condensable gas was discharged from the vessel by flushing CO_2 through the vessel. The vessel was connected to a CO_2 gas bottle. By regulating a precise control valve, the pressure in the vessel could reach a specific value, which was higher than the critical pressure (~7.4 MPa) for CO_2. The CO_2 fluid in the vessel was cooled by a helical coiled tube, through which cold water flowed, keeping the CO_2 fluid at a specific bulk fluid temperature T_b. Two sapphire glass windows were arranged on the vessel to ensure that light passed through the CO_2 fluid for visual observation. T_b of CO_2 was measured by a sheathed thermocouple inserted into the vessel. A metal wire was positioned horizontally and perpendicular to the axial direction of the pressure vessel (see Fig. 1b-c). The wire was connected to an external electric circuit to act both as a heat source and temperature sensor. The wire was tightly fixed to two electrodes to apply a direct-current (DC) voltage in the electric circuit; hence, the wire was kept straight without bending at room temperature.

2.1.2. Operating conditions

The fluid pressure P was kept at ~8 and ~10 MPa [9], both of which are clearly higher than the critical pressure. T_b was controlled at 288.2 K. A Pt wire and a Ni-Cr wire were used in the study. Both wires had a length of 22.0 mm and a diameter of 70 μm. The experiments covered a wide range of operating conditions, with heat fluxes in the range of 25–917 kW/m^2 and wall superheating ΔT_w in the range of −12–850 K. Here, ΔT_w is the wall temperature T_w minus the pseudo-critical temperature T_{pc}, i.e., $\Delta T_w = T_w - T_{pc}$. The density of the supercritical fluid would vary significantly in the direction normal to the heating wall. Our previous studies revealed a darker color in the lighter fluid region, and brighter color in the heavier fluid region [9]. The interface thus formed between the darker and brighter regions was defined as the pseudo-interface, which was captured by a camera and processed using the grey extraction method [9]. Thus, the thickness of the vapor-like-layer was measured [9]. The results show that only the EL

Table 1
Natural convection experiments of sCO_2 in the literature.

Symbol	Ref.	Wire materials and size	P (MPa)	T_b (K)	q_w (kW/m^2)	ΔT_w (K)	Findings and comments
□	[10]	Ni-Cr and Pt/ 25.4 μm, 76.2 μm	7.5~ 9.6	283.2–306.2	29–493	−30–250	Figs. 3,5,6,8,10 show the nonmonotonic variation of heat transfer coefficients versus wall temperatures.Fig. 5 demonstrates the improved heat transfer when increasing pressures.
○	[15]	Pt / 76 μm, 380 μm	6.3–7.8	305.2	0–1000	0–1000	Measurement of the heat transfer to CO_2 over a pressure range from 0.8 P_c to 1.1 P_c are reported. The heat transfer at supercritical pressures is similar to the film boiling at subcritical pressures.
△	[16]	Pt /254 μm	7.58	298.2–314.8	0–700	0–840	Experiments of CO_2 heat transfer near the critical point were conducted, including three flow patterns of a usual natural convection, a highly turbulent flow with periodic bubble-like structure, and oscillating flow with bubble-like structure.
▽	[19]	Pt /100 μm	6.42–7.41	304.4	1–1000	0□1–1000	Boiling is continued from subcritical pressure to a pressure far above the critical point. Surface tension exists even at supercritical pressure under thermal gradient condition.
◇	[20]	Pt / 0.05 mm~0.3 mm	7.4–9.5	283.2–323.2	0–100	−25–40	Experiments of CO_2 convection heat transfer was performed over moderate wall superheating. Nusselt number is correlated based on the classical form by introducing additional correction terms, which are the functions of dimensionless temperatures such as $(T_{pc}-T_b)/T_c$.
☆	[9]	Ni-Cr and Pt /70 μm	8.0–10.0	288.2	60–1700	0–850	Both Pt and Ni-Cr wires were used as the heater and temperature sensor. Pseudo-evaporation mode is observed for the Pt wire, but both pseudo-evaporation mode and boiling-like mode are observed for the Ni-Cr wire. The mechanism for the observed phenomena is explored.

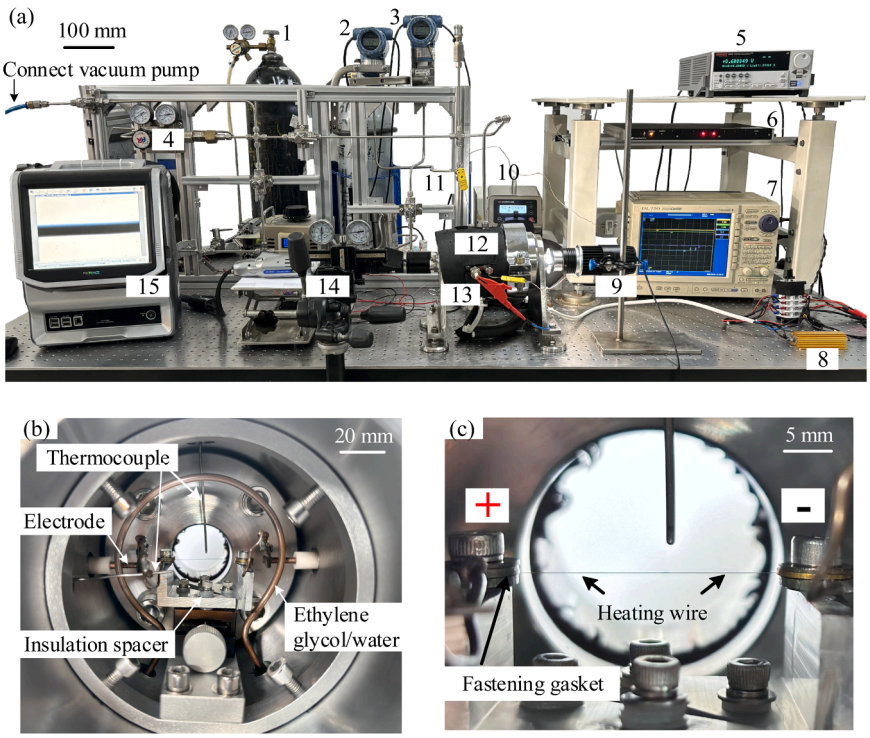


Fig. 1. Experimental setup [22]. (a) Photo of the experimental setup (1. high purity carbon dioxide bottle, 2. pressure transmitter, 3. vacuum transmitter, 4. vent valve, 5. pulse DC voltage generator, 6. synchronizer, 7. high speed data acquisition system, 8. reference resistance, 9. circulating pump, 11. thermocouple, 12. high pressure vessel, 13. electrode, 14. high speed camera, 15. display of high-speed camera); (b) Image focusing on internal structure of the high-pressure vessel; (c) Fixing details of platinum wire. [22], Copyright 2026, Elsevier.

mode was identified for the Pt wire. As a stable heat transfer mode, the EL mode exhibited a vapor-like layer on the wire surface, beyond which was the bulk fluid region [9]. The experimental data for the Pt wire were used as the reference data for comparison with numerical simulations. For the Ni-Cr wire, three modes, namely the EL, TEB, and BL modes were observed [9]. Because the BL mode involves piston-motion-induced bubble-like structures [9], the outcomes related to the BL mode are not discussed here.

2.1.3. Data reduction and uncertainty analysis

The electrical resistivity of the wire ρ_{Pt} is experimentally determined as [9]:

$$\rho_{Pt} = 1.078 \times 10^{-7} \times \left(1 + 3.908 \times 10^{-3} T_w\right), \tag{1}$$

where T_w is the heater temperature, with the unit of °C. The electric resistance R_h, with the unit of Ω, Joule heating power Q_h, with the unit of W, and internal heat source intensityϕ_h, with the unit of W/m^3, are as follows [9]:

$$R_h = \rho_{Pt}\frac{L}{A}, Q_h = \frac{U_h^2}{R_h}, \phi_h = \frac{U_h^2}{\rho_{Pt} L^2}, \tag{2}$$

where A is the cross-sectional area of the heater wire, given by$A = 0.25\pi D_0^2$; D_0 is the heater diameter; L is the heater length; and U_h is the voltage applied to the heater wire, with the unit of V.

When steady state is reached, the surface heat flux q_w is calculated as follows:

$$q_w = \frac{Q_h}{\pi D_0 L}. \tag{3}$$

The heat transfer coefficient h and Nusselt number **Nu** are calculated as [1]:

$$h = \frac{q_w}{T_w - T_b}, \mathbf{Nu} = \frac{hD_0}{\lambda}, \tag{4}$$

where T_b is the bulk fluid temperature and λ is the thermal conductivity of CO_2 evaluated at the reference temperature $T_r = 0.5(T_w + T_b)$.

The signals of U_h and T_b were recorded by a high-speed data acquisition system (DL750, Yokogawa, Japan). U_h and T_b measurements had uncertainties of 0.5% and 0.2 °C, respectively. P was measured using a pressure transducer (Rosemount 3051), with a response time of approximately 10 ms and an uncertainty of 0.075%. The errors in q_w and h were obtained using the error transmission principle [23]; these were 1.74% and 4.84% for q_w and h, respectively. Table 2 summarizes the ranges, uncertainties, and response times for various parameters.

2.2. Numerical simulations of supercritical NCHT

Fig. 2a shows the physical model extracted from the experiments [9]. Pure CO_2 was contained in the horizontal pressure vessel, with its pressure and bulk temperature controlled steadily at P and T_b. The Pt wire acted as both the heater and temperature sensor, with length L and electric resistance R_h. The total DC voltage applied to the circuit was U_t, while the voltage applied across the heater was U_h.

The following assumptions were made for the numerical simulations:

Table 2
Parameter measurements and uncertainties [9].

Parameter	Range	Error	Response time
pressure P	7.955–10.035 MPa	0.075%	< 100 ms
pool fluid temperature T_b	14.9–15.1 °C	0.1 °C	< 250 ms
voltage U_h	0–19 V	0.5%	< 1 μs
wire temperature T_w	15–850 °C	3.71%	< 1 μs
heat flux density q_w	0–1822.0 kW/m^2	1.74%	< 1 μs
heat transfer coefficient h	0–4703.8 kW/(m^{2}K)	4.84%	< 1 μs

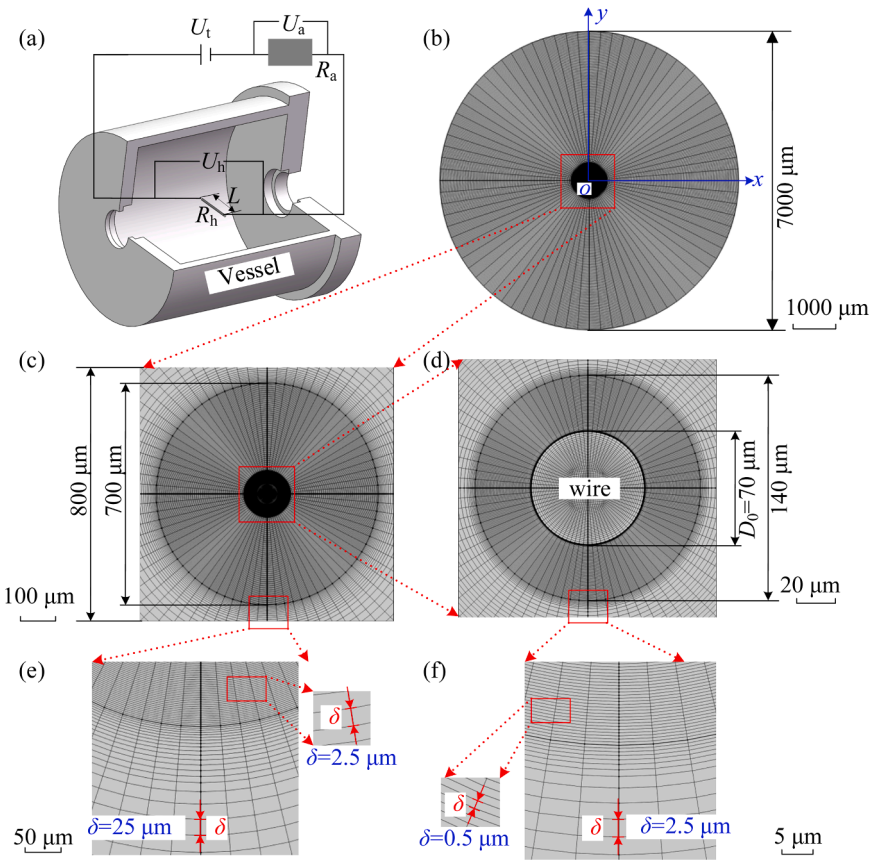


Fig. 2. Physical model and cell generation (a: the physical model extracted from experiments, b, c, d, e and f show the cell generation with total cell elements of 32880.).

(i) Steady-state natural convection heat transfer was attained, which was of interest for the comparison between the simulation and experimental results. However, transient flow and heat transfer were modeled assuming that the heat flux would begin to be applied to the heater at an initial time of $t = 0$. The computation was stopped after a sufficiently long duration of t_{end}, so that steady state could be reached. (ii) Because the heater had a sufficiently large length-to-diameter ratio (L/D_0) of 314, which exceeded the criterion (a value of 200) reported in the literature for natural convection [24], axial heat conduction along the heater and heat transfer from the heater to the supporting structure were considered negligible; hence the problem was treated as a two-dimensional one. (iii) To consider the non-uniform temperature distribution in the heater wire, solid–fluid coupling was considered. (iv) The physical properties of CO_2 were taken from NIST software [25]. At each operating pressure, the physical properties were extracted from this software at a small temperature interval of 0.01 K. These data were embedded into COMSOL software and accessed by the same at each iteration of the numerical simulation. The computation domain was discretized with non-uniform cells. To ensure high resolution and stability of the numerical simulations, fine cells were setup near the wire region, which were gradually enlarged toward the bulk fluid region.

2.2.1. Governing equations

Transient fluid–solid coupling was considered for the computation, and the governing equations for the same are described here. The wire was so thin that the Rayleigh number **Ra** was in the range of 446–16941, which was below the laminar-to-turbulent transition criterion of 10^9 [26]. Hence, the laminar flow and heat transfer model was applied. Considering variations in the physical properties, the 2D governing equations in the fluid domain can be written as [1]:

$$\frac{\partial(\rho u)}{\partial x}+\frac{\partial(\rho v)}{\partial y}=0, \tag{5}$$

$$\frac{\partial(\rho u)}{\partial t}+\frac{\partial(\rho uu)}{\partial x}+\frac{\partial(\rho uv)}{\partial y}=-\frac{\partial P}{\partial x}+\frac{\partial}{\partial x}\left(\mu\frac{\partial u}{\partial x}\right)+\frac{\partial}{\partial y}\left(\mu\frac{\partial u}{\partial y}\right), \tag{6}$$

$$\frac{\partial(\rho v)}{\partial t}+\frac{\partial(\rho uv)}{\partial x}+\frac{\partial(\rho vv)}{\partial y}=-\frac{\partial P}{\partial y}+\frac{\partial}{\partial x}\left(\mu\frac{\partial v}{\partial x}\right)+\frac{\partial}{\partial y}\left(\mu\frac{\partial v}{\partial y}\right)+\rho g, \tag{7}$$

$$\frac{\partial(\rho c_p T)}{\partial t}+\frac{\partial(\rho c_p uT)}{\partial x}+\frac{\partial(\rho c_p vT)}{\partial y}=\frac{\partial}{\partial x}\left(\lambda\frac{\partial T}{\partial x}\right)+\frac{\partial}{\partial y}\left(\lambda\frac{\partial T}{\partial y}\right), \tag{8}$$

where x and y are the two coordinates (see Fig. 2b); u and v are the velocities along the x and y coordinates, respectively; P is the pressure; ρ is the density; μ is the dynamic viscosity; c_p is the specific heat; λ is the thermal conductivity; g is the gravitational acceleration (g= 9.81 m^2/s).

Heat conduction within the wire obeys the following Eq. [1]:

$$\rho_w c_{p,w}\frac{\partial T}{\partial t}=\frac{\partial}{\partial x}\left(\lambda_w\frac{\partial T}{\partial x}\right)+\frac{\partial}{\partial y}\left(\lambda_w\frac{\partial T}{\partial y}\right)+\phi_h, \tag{9}$$

Where subscript w denotes the wire in the solid domain. The physical properties of the wire were set for Pt. The no-slip boundary condition yields the continuity of temperature and heat flux at the solid–fluid interface as:

$$T_w=T_f, \lambda_w\frac{\partial T_w}{\partial n}=\lambda_f\frac{\partial T_f}{\partial n}, \tag{10}$$

where subscript f represents the fluid CO_2; n is the normal coordinate perpendicular to the solid–fluid interface.

2.2.2. Numerical method

The laminar flow and heat transfer of sCO_2 coupled with the solid wire was numerically investigated using the commercial Multiphysics software COMSOL. The physical properties of sCO_2 were extracted from NIST software. The numerical method, including the computation domain with non-uniform cells, initial and boundary conditions, iteration and data process are as follows.

Computational domain with non-uniform cells: The computational domain, including a center-wire sub-domain and fluid sub-domain, comprised a circular region with a diameter of 7000 μm, which was 100 times the wire diameter (see Fig. 2b). In the circumferential direction, the domain was uniformly discretized into 80 elements, corresponding to a circumferential angle $\Delta\theta$ of 4□5°□ Three grades of cells were used to achieve the non-uniform resolution in the radial direction (see Fig. 2c-f), dividing the computational domain into three regions: (i) cell size (δ) was 0.5 μm in the first region with $D < 140$ μm, including a 70 −μm subregion for the wire and another 70 −μm subregion for the fluid. Beyond $D = 140$ μm, δ was gradually enlarged from 0.5 to 2.5 μm. (ii) δ was 2.5 μm in the majority of the second region with $140 < D < 700$ μm. Beyond $D = 700$ μm, δ was gradually enlarged from 2.5 to 25 μm. (iii) δ was 25 μm in the third region of $D > 700$ μm.

Initial and boundary conditions: For the transient simulation, initial conditions were set to zero for the u and v velocity components and T_b in the whole computational domain. Eq. (10) specifics the boundary condition at the solid-fluid interface. It was assumed that at the outer boundary of $D = 7000$ μm, T_b and velocities were again zero. The present problem involved solid–fluid coupling. Because U_h was treated as an input parameter, the wire temperature T_w and Joule heating intensity ϕ_h were coupled.

Two levels of iteration processes: For the numerical simulation, the input parameters included U_h, L, D_0, and the thermophysical properties of Pt and CO_2. Next, a non-uniform cell structure was constructed (see Fig. 2) and the initial conditions at $t = 0$ were assigned (see Fig. 3). The total simulation time was 100 s, with a maximum time step of 0.01 s. The computation involved two levels of iteration (see Fig. 3). The first level of iteration was related to the transient simulation by advancing the time step consecutively, until a sufficiently long physical time t_{end} was reached, at which the computation outcomes would not change with time. The second level of iteration was to achieve stabilized outcomes of flow and temperature fields over the whole computational domain at each time step. After the computation at a current iteration step was completed, the velocities and temperatures in each cell at this iteration were compared with those at the previous iteration, generating the residual error (ε)□ If ε was smaller than a prescribed value, for example, 10^{-5}, convergence was supposed to have been reached; then the computation would proceed to the next time step. Otherwise, a new iteration would begin. Because the Joule heating and temperatures of the heater were updated after each iteration, the second level of iteration would account for the solid–fluid coupling.

Verification of cell-size independence: The number of cells shown in Fig. 2 is 32,880. Before the final outcomes were achieved, a sensitivity analysis was performed. Fig. 4a shows the effect of the number of cells on T_w. With 15,000 cells (coarse mesh), T_w reached 573.0 K. When the number of cells was more than 30,000, T_w stabilized at 572.3 K and did not change further. The temperature variation on the cross-section of the heater wire may also be of interest. For the cases shown in Fig. 4b, the temperature difference over the whole cross-section was smaller than 0.3 K. Notably, the maximum temperature was not located at the wire center, due to the small difference in the heat transfer coefficients along the circumferential direction of the heater wire. Hence, neglecting the temperature variation inside the heater wire resulted in minor uncertainties; however, the solid–fluid coupling computation was still used in this study.

The classical definition of Rayleigh number **Ra** is as follows [1]:

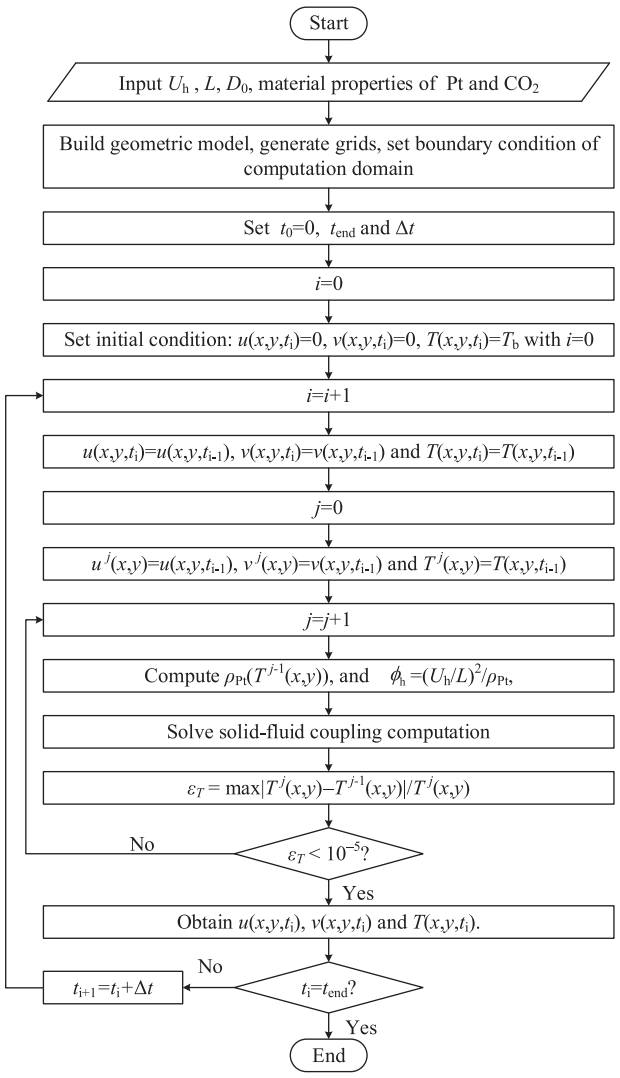


Fig. 3. The solid-fluid-coupling numerical simulation scheme.

$$\mathbf{Ra} = \frac{g\beta(T_w - T_b)D_0^3}{va}. \tag{11}$$

The volume expansion coefficient β is an important parameter to characterize the buoyancy effect. Natural convection takes place owing to the difference between T_w and T_b. β was taken from Ref. [20], which is as follows:

$$\beta = \left(-\frac{1}{\rho}\frac{\Delta\rho}{\Delta T}\right) = \frac{\rho_b - \rho_w}{\rho(T_w - T_b)}. \tag{12}$$

In Eqs. (11) and (12), ν is the kinematic viscosity; a is the thermal diffusivity; and ρ is the density; these were determined at the reference temperature $T_r = 0.5(T_w + T_b)$ [1]. ρ_b and ρ_w are the densities at the bulk fluid temperature T_b and wall temperature T_w, respectively.

3. Results and discussion

3.1. Experimental and simulation results of supercritical NCHT

Table 3 lists the experimental data and simulation results for sCO_2, comprising 63 data sets. The data at $P = 8$ and 10 MPa are presented for comparison between the experiments and simulations; however, numerical simulation results only are presented at $P = 12$, 14, and 16 MPa. A graphical comparison of simulations and experiments is shown in

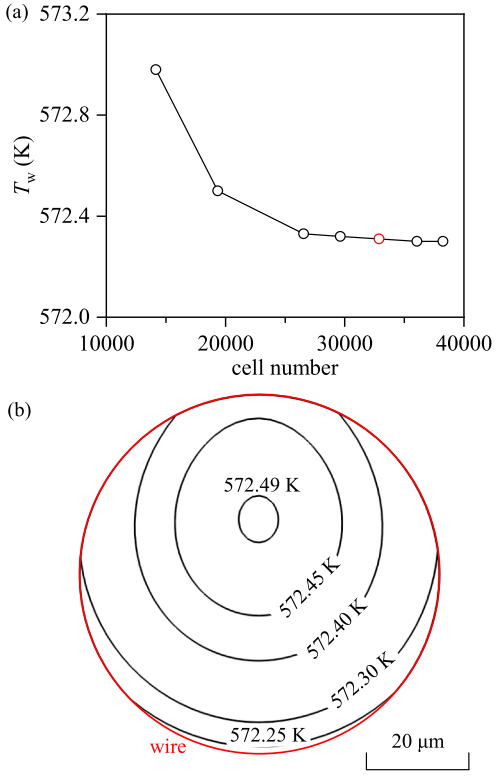


Fig. 4. Effect of cell number on wire temperatures with $P = 10$ MPa, $T_w = 572.3$ K, and $q_w = 550.86$ kW/m^2 (a), and temperature distribution over the cross-section of the heater wire (b).

Fig. 5, with ΔT_w along the horizontal coordinate, and q_w, h, and **Nu** along the three vertical coordinates in Figs. 5a, 5b, and 5c, respectively. The results in Fig. 5 are for sCO_2 with $T_b = 288.2$ K, $L = 22.0$ mm and $D_0 = 70$ μm. The experimental setup can be seen in Section 2.1. Here, P, q_w, T_w and ΔT_w span cover ranges of (8−16) MPa, (112−917) kW/m^2, (305−672) K, and (−21–332) K, respectively. Notably, the numerical simulation results matched the experimental data very well. Importantly, both simulations and experiments demonstrated non-monotonic change of h and **Nu** versus ΔT_w, i.e., h increased sharply to reach a peak value with ΔT_w in a narrow range from negative values up to 16.2–22.3 K, then decreased to a constant value when ΔT_w exceeded 200 K. Thus, the data are marked in red to exhibit the sharp rising trend, under which natural convection dominated. The data beyond the peak point are marked in black to show the decreasing trend, under which mechanisms other than natural convection may have existed that deteriorate heat transfer. **Nu** illustrated a trend similar to that of h; however, the transition wall superheating at the peak points were different between the h and **Nu** curves.

The non-monotonic variation trend identified in this work was consistent with the supercritical heat transfer trend reported by earlier studies [10,11]. In these studies, Pt wires ranging in size from 25.4 to 100 μm and a Ni-Cr wire of 101.6 μm diameter were used. The P and T_b were varied in the ranges of 6.34–9.60 MPa and 10.0–33.3 °C, respectively. T_w was systematically increased from T_b + 0.1–250 °C. The present results of Fig. 5 match the trend shown in Figs. 3, 5, and 6 in the experimental work [10], and Figs. 8 and 10 in the simulation work [10]. Besides, Fig. 5 in this paper indicates elevated heat transfer coefficients with pressure increasing from 8 to 10 MPa, which is also supported by the finding illustrated in Refs. [10,11].

Fig. 6 plots the flow and temperature fields for cases a, b and c marked in Fig. 5b. The three cases correspond to $\Delta T_w = -6.51$ K, 22.26 K corresponding to the peak h, and $\Delta T_w = 131.32$ K, respectively. The natural-convection-induced velocities increased with increase in ΔT_w from case a to case c. For case a, due to a low ΔT_w, the pseudo-critical temperature did not exist in the whole temperature field; however, for the cases b and c, a red envelope, in which the temperature equals to T_{pc} did exist to include a circular part and an upward plume part surrounding the wire. Temperatures were higher than T_{pc} in the red envelope and lower than T_{pc} beyond the red envelope. Special attention should be paid to the velocities in the red envelope. On the one hand, flow velocities were not developed in the envelope due to the no-slip temperature boundary condition at the wire surface. On the other hand, the horizontally positioned wire blocked the development of near-wall flow field. Especially, the flow was blocked below the lower surface of the wire. The flow and temperature fields presented in Fig. 6 help us develop a two-region model that accounts for the vapor-like-layer effect.

3.2. Scaling law of supercritical NCHT

Both the present study and previous studies [10,11] indicate that the heat transfer behavior varies non-monotonically with wall superheating, conflicting with the monotonic variation of heat transfer versus wall superheating at subcritical pressures reported elsewhere [5–7]. This contradiction inspired us to develop a physical model to consider the vapor-like-layer-induced film boiling effect. The flow and temperature patterns presented in Fig. 6 are summarized in the physical model shown in Fig. 7a. The core idea was to divide the domain into a vapor-like-region and a bulk fluid region. Due to the low velocities in the vapor-like-region, only thermal conduction was considered. On the other hand, natural convection was considered in the bulk fluid region, whose temperatures ranged from T_{pc} to T_b. Hence, a modified Rayleigh number $\mathbf{Ra}_m$ was defined as:

$$\mathbf{Ra}_m = \frac{g\beta(T_{pc} - T_b)D_S^3}{\nu a}, \tag{13}$$

where D_S is the equivalent diameter of the vapor-like-layer envelope, $D_S = 2R_S$; ν and a are characterized by the reference temperature $T_r = 0.5(T_{pc} + T_b)$; and β is calculated as:

$$\beta = \left(-\frac{1}{\rho}\frac{\Delta\rho}{\Delta T}\right) = \frac{\rho_b - \rho_{pc}}{\rho(T_{pc} - T_b)}, \tag{14}$$

where ρ is characterized by $T_r = 0.5(T_{pc} + T_b)$.

The total thermal resistance R_t consists of R_{VL} in the vapor-like layer and R_{NC} in the bulk fluid region (see Fig. 7a):

$$R_t = R_{VL} + R_{NC}, R_t = \frac{T_w - T_b}{q_w}, R_{VL} = \frac{T_w - T_{pc}}{q_w}. \tag{15}$$

A new parameter, termed the vapor-like-layer resistance ratio $\mathbf{\Theta}$, was defined as follows:

$$\mathbf{\Theta} = \frac{R_{VL}}{R_t} = \frac{T_w - T_{pc}}{T_w - T_b}. \tag{16}$$

It may be noted that the vapor-like-layer structure, including a circular part connected with a plume, influenced the heat transfer. Quantifying the vapor-like-layer size was necessary. The T_{pc} isotherm of Fig. 7a was discretized into a series of nodes to compute the envelope area using the Shoelace formula [27]:

$$S = \frac{1}{2}\left|\sum_{i=1}^{n}(x_i y_{i+1} - x_{i+1}y_i)\right|, x_{n+1}y_{n+1} = x_1 y_1, \tag{17}$$

where (x_i, y_i) and (x_{i-1}, y_{i-1}) are the coordinates of adjacent nodes (see in Fig. 7a).

The number of nodes in the simulation was set to 20000 to ensure sufficient calculation accuracy. The irregular white area including the wire cross-section was then converted into a standard circle with an equivalent radius $R_S = \sqrt{S/\pi}$. Thus, the vapor-like-layer size effect number was defined as $\mathbf{R}_S^* = R_S/R_0$, where R_0 is the wire radius ($R_0 = 0.5D_0$). Using the 63 groups of data listed in Table 3 covering an identical test section and operating parameters of Fig. 5, the $\mathbf{R}_S^*$ data with

Table 3
Experimental and simulation outcomes of sCO_2 with T_b= 288.2 K, L= 22.0 mm and D_0 = 70 μm.

No.	P (MPa)	q_w (kW/m^2)	T_w (K)	ΔT_w (K)	$\mathbf{Nu}_{exp}$	$\mathbf{Nu}_{sim}$	$\mathbf{Ra}_m$	$\boldsymbol{\Theta}$	R_S/R_0	De
1	8	112.9	334.3	26.5	3.40	3.55	2229.0	0.57	1.50	0.38
2	8	133.1	344.6	36.7	4.47	4.44	2974.0	0.65	1.66	0.39
3	8	140.3	348.5	40.7	4.54	4.61	3295.9	0.67	1.71	0.39
4	8	158.0	358.3	50.4	4.76	4.88	4232.1	0.72	1.86	0.39
5	8	177.2	368.8	61.0	5.20	5.04	5422.7	0.76	2.02	0.37
6	8	199.2	382.5	74.6	4.96	5.05	7306.0	0.79	2.23	0.35
7	8	210.1	389.3	81.4	5.11	5.04	8446.9	0.81	2.34	0.34
8	8	237.8	409.9	102.0	5.00	4.84	12168.9	0.84	2.65	0.32
9	8	251.2	420.3	112.5	4.90	4.72	14247.3	0.85	2.79	0.30
10	8	264.9	430.5	122.6	4.75	4.63	16135.3	0.86	2.91	0.30
11	8	303.0	457.8	150.0	4.70	4.40	21950.7	0.88	3.22	0.27
12	8	308.4	461.9	154.0	4.45	4.36	23442.0	0.89	3.29	0.27
13	8	327.3	475.4	167.6	4.34	4.25	25819.1	0.89	3.40	0.26
14	8	344.0	485.7	177.9	4.33	4.21	29692.9	0.90	3.56	0.25
15	8	384.9	512.7	204.8	4.19	4.05	37744.1	0.91	3.86	0.24
16	8	422.5	537.1	229.3	4.06	3.91	44389.6	0.92	4.08	0.23
17	8	475.9	568.3	260.5	3.92	3.80	56048.2	0.93	4.41	0.21
18	8	527.9	596.2	288.3	3.76	3.73	71581.9	0.94	4.78	0.20
19	10	151.2	340.4	22.3	2.94	2.89	1730.0	0.43	1.43	0.30
20	10	178.2	354.6	36.5	3.29	3.30	2547.5	0.55	1.63	0.34
21	10	203.0	371.2	53.0	3.94	4.04	3549.9	0.64	1.82	0.35
22	10	216.2	380.2	62.1	4.21	4.26	4151.6	0.67	1.91	0.35
23	10	230.1	388.1	69.9	4.45	4.42	4703.7	0.70	1.99	0.35
24	10	255.5	402.4	84.3	4.54	4.59	5817.4	0.74	2.14	0.34
25	10	271.8	411.5	93.3	4.62	4.66	6593.8	0.76	2.23	0.34
26	10	301.0	428.7	110.5	4.60	4.68	8257.0	0.79	2.41	0.33
27	10	337.6	449.5	131.3	4.64	4.67	10643.7	0.81	2.62	0.31
28	10	380.2	473.9	155.8	4.55	4.59	14016.1	0.84	2.87	0.29
29	10	419.5	497.9	179.7	4.44	4.46	17993.2	0.86	3.12	0.27
30	10	465.2	522.0	203.9	4.36	4.38	22685.5	0.87	3.37	0.26
31	10	509.4	546.4	228.2	4.26	4.28	27997.3	0.88	3.61	0.24
32	10	558.9	574.0	255.8	4.13	4.16	33812.8	0.89	3.85	0.23
33	12	181.6	348.5	21.4	/	2.94	1072.2	0.35	1.26	0.28
34	12	198.3	355.4	28.3	/	3.05	1250.4	0.42	1.33	0.32
35	12	222.4	365.6	38.4	/	3.27	1529.9	0.50	1.41	0.35
36	12	245.5	378.8	51.7	/	3.58	1808.6	0.57	1.50	0.38
37	12	257.8	381.5	54.4	/	3.76	1982.5	0.58	1.55	0.38
38	12	291.4	397.5	70.3	/	4.23	2515.0	0.64	1.67	0.38
39	12	332.1	417.5	90.4	/	4.60	3308.5	0.70	1.83	0.38
40	12	360.7	431.8	104.7	/	4.75	3968.3	0.73	1.95	0.37
41	12	401.2	452.2	125.0	/	4.85	5103.9	0.76	2.12	0.36
42	12	458.6	481.1	154.0	/	4.86	7148.1	0.80	2.37	0.34
43	12	484.3	494.0	166.9	/	4.84	8246.5	0.81	2.49	0.33
44	12	537.9	520.7	193.5	/	4.77	10953.9	0.83	2.73	0.30
45	12	596.5	549.2	222.1	/	4.68	14615.6	0.85	3.01	0.28
46	12	630.3	565.5	238.3	/	4.62	17055.4	0.86	3.17	0.27
47	12	691.5	594.5	267.4	/	4.51	22084.9	0.87	3.45	0.25
48	16	262.4	378.1	37.9	/	2.95	1016.6	0.42	1.35	0.31
49	16	285.0	387.3	47.0	/	3.09	1182.2	0.47	1.42	0.33
50	16	305.2	395.7	55.5	/	3.22	1344.5	0.52	1.48	0.35
51	16	337.0	409.5	69.3	/	3.45	1633.0	0.57	1.58	0.36
52	16	359.5	419.5	79.3	/	3.61	1861.8	0.60	1.65	0.36
53	16	394.4	435.5	95.2	/	3.84	2266.8	0.65	1.77	0.37
54	16	444.1	458.5	118.2	/	4.10	2948.4	0.69	1.93	0.36
55	16	488.8	479.4	139.2	/	4.25	3697.1	0.73	2.08	0.35
56	16	541.1	503.7	163.5	/	4.36	4768.0	0.76	2.26	0.34
57	16	587.6	525.3	185.1	/	4.40	5911.9	0.78	2.43	0.32
58	16	671.3	563.4	223.1	/	4.42	8503.9	0.81	2.74	0.30
59	16	740.8	594.5	254.2	/	4.39	11281.3	0.83	3.01	0.28
60	16	773.8	610.2	269.9	/	4.36	12891.7	0.84	3.15	0.27
61	16	821.6	630.0	289.8	/	4.33	15215.6	0.85	3.33	0.25
62	16	867.3	651.0	310.8	/	4.26	18000.3	0.86	3.52	0.24
63	16	917.2	672.4	332.2	/	4.21	20891.5	0.86	3.70	0.23

four pressures of 8, 10, 12 and 16 MPa were coincided with a single curve, showing an increasing trend with increase of $\boldsymbol{\Theta}$ (see Fig. 7b). Besides, the slope of the $\mathbf{R}_S^*$ curve is gentle when $\boldsymbol{\Theta} < 0.6$, but increases sharply when $\boldsymbol{\Theta} > 0.6$. Using $\mathbf{R}_S^*$ and $1 - \boldsymbol{\Theta}$ as the two coordinates, the curve is replotted in Fig. 7c. The best curve fitting gave the scaling law as follows:

$$\mathbf{R}_S^* = \frac{R_S}{R_0} = 0.93(1 - \boldsymbol{\Theta})^{-0.59}. \tag{18}$$

Physically, $\mathbf{R}_S^*$ represents the degree of expansion of the vapor-like-layer relative to the heater. Noting that $1 - \boldsymbol{\Theta} = (T_{pc} - T_b)/(T_w - T_b)$ and T_{pc} is solely dependent on P, $\mathbf{R}_S^*$ is comprehensively determined by parameters T_w, T_{pc}, and T_b (see Fig. 7c). The self-similarity characteristic of $\mathbf{R}_S^*$ is further verified in Fig. 8. The three cases in each subfigure share

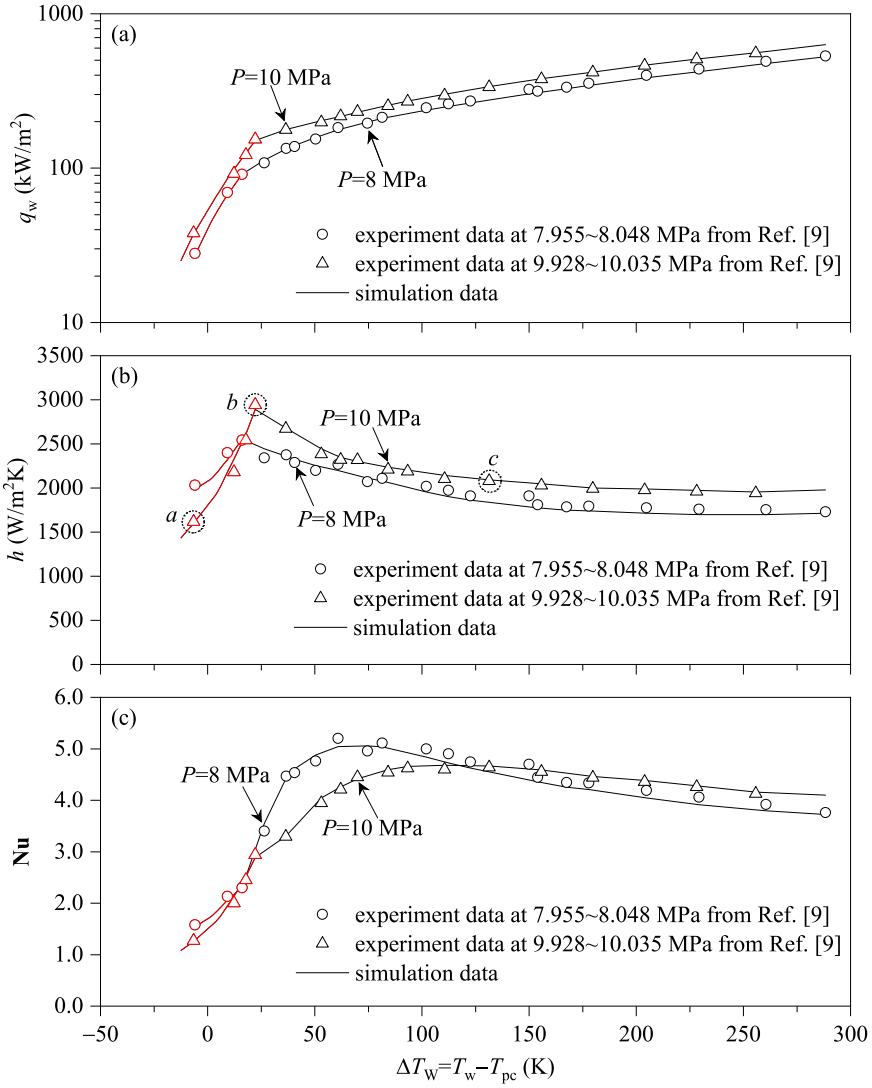


Fig. 5. Comparison of numerical simulations with experiments (a: heat fluxes q_w versus wall superheating ΔT_w; b: heat transfer coefficients h versus wall superheating ΔT_w; c: Nusselt number **Nu** versus wall superheating ΔT_w.).

identical **Θ**. Even though these cases had different pressures, wall temperatures and heat fluxes, the vapor-like-layer morphologies were very similar, providing **Θ** was the same. However, the morphology became thicker with increasing **Θ** as observed from a comparison of the three subfigures of a, b and c.

Now, the effectiveness of the non-dimensional parameters was examined to explain the non-monotonic behavior of supercritical natural convection. Again, the data in Table 3 were used for the presentation. The test section and ranges of parameters, such as P, q_w, T_w, and ΔT_w in Fig. 9 are identical to those of Fig. 5. Fig. 9a plots the classical **Ra** versus ΔT_w. The parabolic distribution of **Ra** curves contradicts the fact that **Ra** should increase with increase in T_w. In other words, the classical **Ra** is only suitable for low T_w values without the vapor-like-layer effect. When the vapor-like-layer effect becomes stronger at higher ΔTw values, **Ra** cannot capture the natural convection mechanism. Correspondingly, the **Nu** ~ **Ra** curves shown in Fig. 9b demonstrate the loop-back phenomenon for the P = 8, 10, 12, and 16 MPa. Initially, marked by the red symbols, as **Ra** increased due to an increase in ΔT_w, **Nu** also increased. When $\Delta T_w > 0$, both **Ra** and **Nu** reached their maximum values. Marked by the black symbols, further increase in ΔT_w resulted in decreases in both **Ra** and **Nu**; however, **Ra** and **Nu** did not peak at the same value of ΔT_w. Thus, the **Nu** ~ **Ra** curve loops back upon itself, which is similar to that observed by He et al. [9]. Essentially, based on the classical definition of **Ra**, **Nu** does not obey the scaling law of **Nu** ~ **Ra**^{c}. Based on the new definition of **Ra**$_m$ expressed in Eq. (13), **Ra**$_m$ exhibits monotonic increase versus ΔTw (see Fig. 9c), satisfying the expectation that Rayleigh number should increase when wall temperature increases. The parabolic distribution of the **Nu** ~ **Ra**$_m$ curves shown in Fig. 9d is consistent with the shape of the **Nu** ~ΔT_w curve shown in Fig. 5c.

Notably, the natural convection mechanism was considered in the $T_b < T < T_{pc}$ region. The decreasing trend of **Nu** beyond the peak point inspired us to search for a heat transfer deterioration number **De** in the $T_{pc} < T < T_w$ region. Apparently, **De** should be less than 1, with **Θ** < 1 contributing partially. Another contribution to **De** comes from the scaling law of R_{VL}~$\mathbf{R}_S^*$ and $\boldsymbol{Nu} \sim \left(\boldsymbol{R}_S^*\right)^{-1}$. Hence, as a comprehensive parameter, **De** was defined as:

$$\mathbf{De} = \mathbf{\Theta}\cdot\left(\mathbf{R}_S^*\right)^{-1} = \mathbf{\Theta}/\mathbf{R}_S^* = 1.08\mathbf{\Theta}(1-\mathbf{\Theta})^{0.59}. \tag{19}$$

Using the 63 groups of data presented in Table 3, the best curve fitting yielded:

$$\mathbf{Nu} = 1.92\cdot\mathbf{Ra}_m^{0.22}\mathbf{De}^{1.01}. \tag{20}$$

Because the exponent of **De** is close to 1, the small difference between 1.01 and 1 can be neglected with negligible error, yielding the linear scaling law of **Nu** ~ **De**. Hence, Eq. (20) becomes:

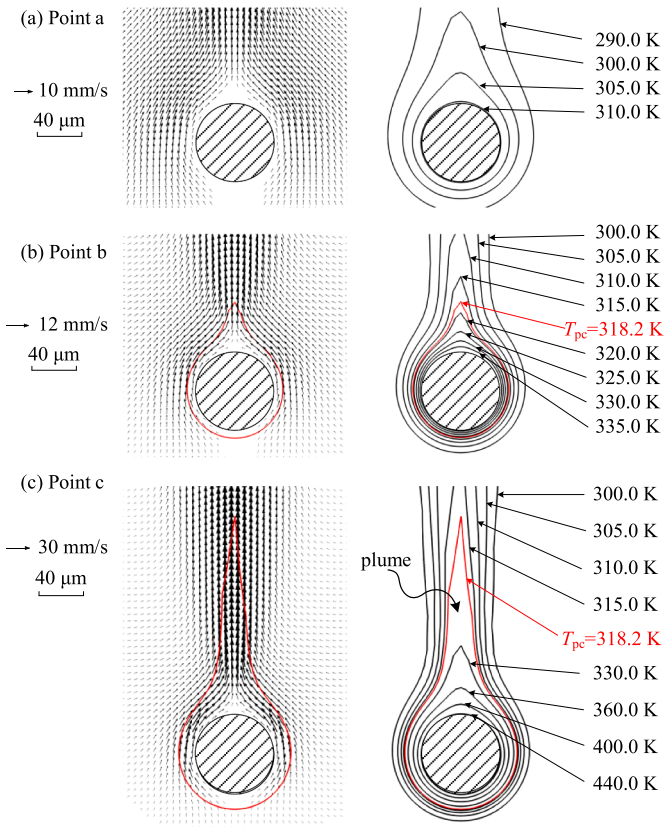


Fig. 6. Velocity and temperature fields at three representative operating points (a: point a; b: point b; c: point c, the three points a, b and c can be referenced to Fig. 5b.).

$$\mathbf{Nu} = 1.92 \cdot \mathbf{Ra}_m^{0.22} \mathbf{De}. \tag{21}$$

In Eq. (21), the natural convection effect is represented by the term $\mathbf{Ra}_m^{0.22}$, and the heat transfer deterioration effect is represented by **De**. To assess the predictive accuracy of Eq. (21), the relative error for each run is defined as follows:

$$e_i = \frac{\mathbf{Nu}_{pre} - \mathbf{Nu}}{\mathbf{Nu}}. \tag{22}$$

The mean relative error e_A, mean absolute relative error e_R, and root-mean-square relative error e_S are as follows:

$$e_A = \frac{\sum_{i=1}^{n} e_i}{n}, e_R = \frac{\sum_{i=1}^{n} |e_i|}{n}, e_S = \sqrt{\frac{\sum_{i=1}^{n} e_i^2}{n}}, \tag{23}$$

where n is the total number of data points, which was 63 for the present evaluation. Again, Fig. 10 shares identical test section and running parameters with Fig. 5. Fig. 10a plots **Nu** versus $\mathbf{Ra}_m^{0.22}\mathbf{De}$, indicating a curve slope of 1.92, Fig. 10b indicates the linear scaling law of **Nu**~**De**. Physically, **De** is smaller than 1. The smaller the value of **De**, the larger the degree of heat transfer deterioration. Fig. 10c illustrates the parabolic distribution of **De** versus ΔT_w. For the four pressures of 8, 10, 12, and 16 MPa, **De** increased sharply to reach a peak value at ΔT_w = 36.7–95.2 K, then gradually decreased with increase in ΔT_w. The data trend shown in Fig. 10c suggests that the degree of heat transfer deterioration was weaker in the small wall-superheating region, but became larger in the high wall-superheating region. The effect of pressures on **De** can also be detected in Fig. 10c, which shows larger **De** with increasing ***P***. In other words, elevating the pressure would improve the heat transfer. Generally, **De** covers a range of 0.20–0.39 to indicate strong vapor-like-layer effect. Fig. 10d presents excellent agreement between the experimental/simulated **Nu** and the correlation-predicted **Nu**, yielding 0.07%, 5.30%, and 6.77%, respectively, for the three errors defined in Eq. (23).

Recalling Fig. 7a, natural convection took place in the bulk fluid region of $T_b < T < T_{pc}$, which was separated from the heater by a vapor-like layer. This process is referred to as indirect natural convection introduced in the present study. On the contrary, natural convection occurring around the heater itself is called the direct natural convection at subcritical pressures. A comparison of the exponent c for direct and indirect natural convection is shown in Fig. 11. In the past, several natural convection experiments were conducted using a horizontally positioned heater and air as the working fluid at subcritical pressures [28–32]; these were summarized by Morgan [5]. Even though the values of the exponent c were scattered, they covered a narrow range from 0.203 to 0.28. Data in Fig. 11 involved Refs. [28–32]. The test section and ranges of the operating parameters are summarized in Table 1 of Morgan [5]. We note that the exponent of 0.22 under supercritical pressures is in the range of those at subcritical pressures, thereby demonstrating a similar natural convection mechanism in the two domains of pressures; however, a significant difference is observed in the vapor-like-layer, which deteriorates the heat transfer in supercritical domain.

3.3. Extension of scaling law to other supercritical fluids and parameter ranges

The scaling law and correlation have been developed based on the 63 sets of data presented in Table 3. Next, we examined whether the scaling law would be applicable to other fluids and parameter ranges. Fig. 12 summarizes the extension of the scaling law to other supercritical fluids and operating parameters, using the data from Tables 3, 4, and 5. The sCO_2 heat transfer data are presented in Table 4 under conditions of T_b = 303.2 K, P = 11 MPa, and D_0 = 140 μm, with q_w, T_w, and ΔT_w covering ranges of 122–505 kW/m^2, 360–632 K, and 38–309 K, respectively. The supercritical water (sH_2O) heat transfer was simulated with P = 25 MPa, T_b = 600.2 K, and D_0 = 70 μm, with q_w, T_w and ΔT_w covering ranges of 917–2912 kW/m^2, 678–1061 K, and 20–403 K, respectively (see Table 5). Water has critical parameters of P_c = 22.1 MPa and T_c = 647.5 K, which are significantly different from those of CO_2. Even though Tables 4–5 were not involved in the correlation development, the three lines were perfectly parallel to one another, demonstrating an excellent scaling law of **Nu** ~ **De**, and indicating its strong applicability to other fluids and parameters (see Fig. 12a). The outcomes of the heat transfer deterioration number **De** are summarized in Fig. 12b. The parabolic distribution of **De** was valid for all the data in Tables 3–5. A higher **De** was observed for sH_2O than for sCO_2, indicating better heat transfer performance of water at supercritical pressures. Fig. 13 highlights the comparison between the present correlation predictions and measured **Nu** reported for sCO_2 heat transfer [8,9,12,13,15,16]. The experimental conditions and findings are summarized in Table 1. Even though these experimental data were not involved in the correlation development, the three errors were small: −4.87%, 14.34%, and 16.83%, respectively. To demonstrate the applicability of the proposed correlation to supercritical NCHT, the iterative procedure to calculate **Nu** and T_w is illustrated in Fig. 14. For given values of P, T_b, and q_w, the bulk fluid properties were first computed. The wall temperature T_w was assumed to compute **Nu** and h using the proposed correlation. Then, $\mathbf{Ra}_m$ and **De** were determined to update **Nu**. Thus, a new wall temperature T_w^* was subsequently calculated. The iteration would proceed until the convergence criterion of $|T_w - T_w^*| \le 10^{-2}$was satisfied.

Summarizing Tables 1, 3, and 4, the scaling law and correlation were valid for sCO_2 with P, T_b, q_w, and ΔT_w covering ranges of 7.4–16.0 MPa, 10–33 °C, 0.9–1718.7 kW/m^2, and 0.7–823.7 K, respectively. The heater diameter covered a range of 25–381 μm. The correlation was also valid for sH_2O heat transfer (see Table 5). In this work, laminar flow and

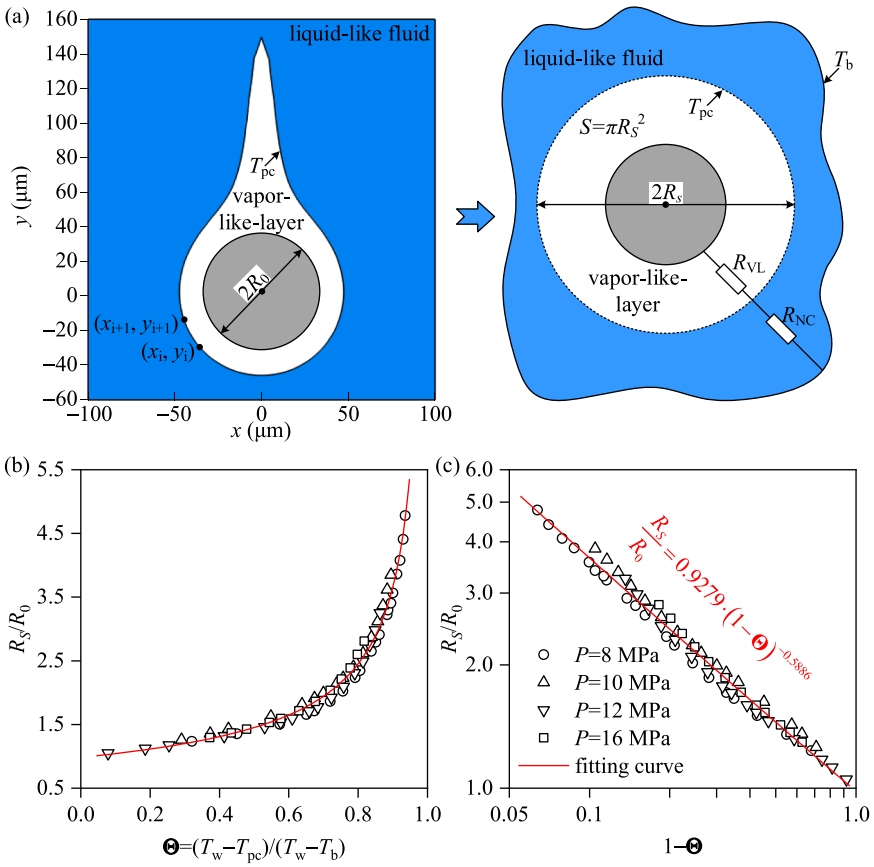


Fig. 7. The physical model (a) and the scaling law of dimensionless vapor-like-layer radius R_S/R_0 with respect to dimensionless temperature difference Θ (b), noting that data for P = 10 MPa, T_w= 402.4 K, and q_w= 252.5 kW/m^2 are used to construct (c).

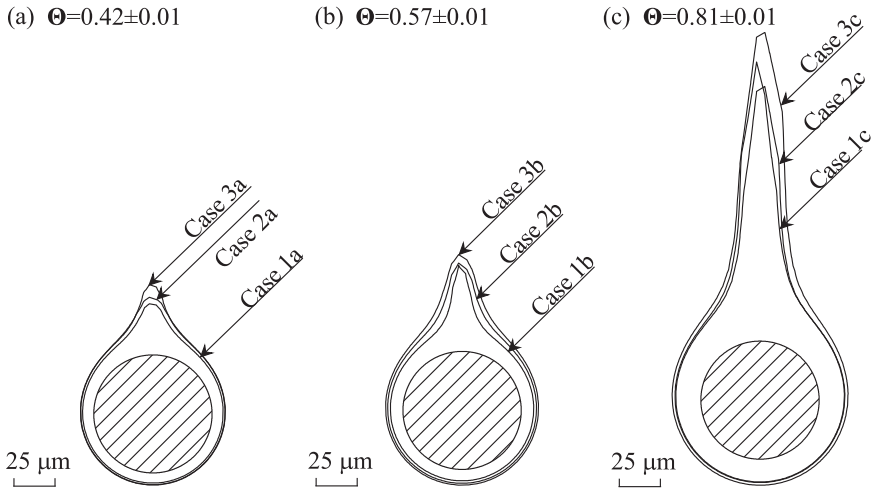


Fig. 8. The self-similarity characteristic of the vapor-like-layer topology at identical Θ for different conditions (a: Θ = 0.42 for cases 1a, 2a and 3a; b: Θ = 0.57 for cases 1b, 2b and 3b; c: Θ = 0.81 for cases 1c, 2c and 3c. case 1a: P = 10 MPa, T_b=288.15 K, T_w=340.42 K, q_w=151.18 kW/m^2; case 2a: P = 12 MPa, T_b=288.15 K, T_w=355.43 K, q_w=198.25 kW/m^2; case 3a: P = 16 MPa, T_b=288.15 K, T_w=378.13 K, q_w=262.35 kW/m^2, case 1b: P = 8 MPa, T_b=288.15 K, T_w=334.32 K, q_w=112.85 kW/m^2; case 2b: P = 12 MPa, T_b=288.15 K, T_w=378.82 K, q_w=245.48 kW/m^2; case 3b: P = 16 MPa, T_b=288.15 K, T_w=409.51 K, q_w=336.98 kW/m^2; case 1c: P = 10 MPa, T_b=288.15 K, T_w=449.48 K, q_w=337.63 kW/m^2; case 2c: P = 12 MPa, T_b=288.15 K, T_w=493.98 K, q_w=484.28 kW/m^2; case 3c: P = 16 MPa, T_b=288.15 K, T_w=563.36 K, q_w=671.26 kW/m^2.).

heat transfer were treated with a horizontally positioned heater having a large length-to-diameter ratio, under which the 3D effect could be neglected. As mentioned earlier, significant efforts have been made to correlate supercritical NCHT using classical **Ra** [10,15–17,20]. The modifications focused on the selection of the reference temperature to characterize the varied physical properties [10,16]. Among these, Goldstein and Aung [16] and Rousselet et al. [10] used reference temperatures of $(T_b + T_w)/2$ and T_b, respectively. Alternatively, Neuman and Hahne [20] introduced an empirical correction factor to consider the strong variable-property effect. In contrast to these studies, the

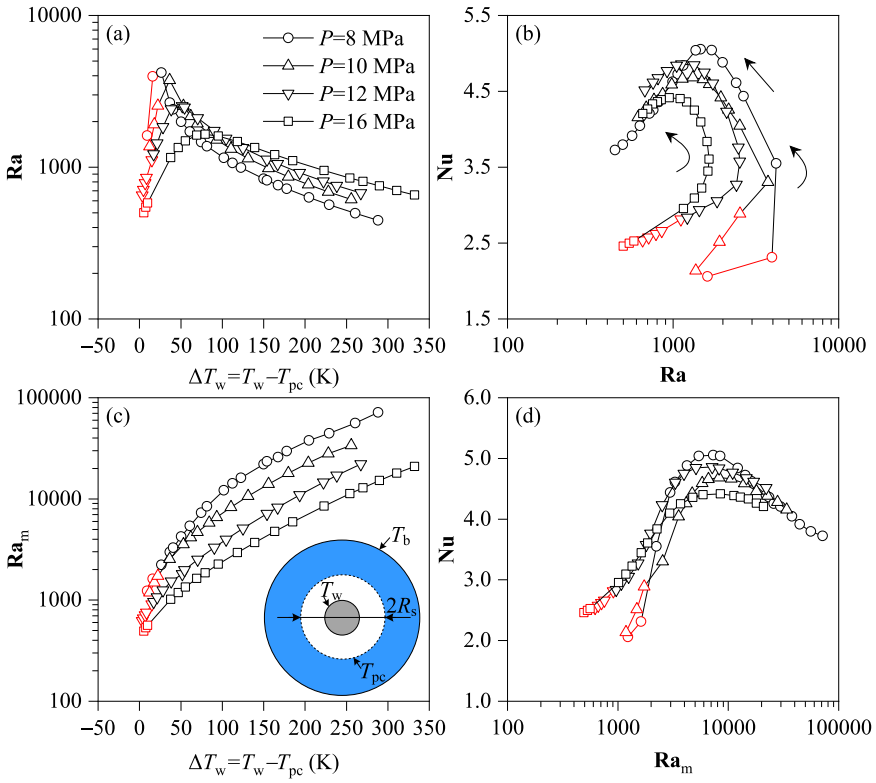


Fig. 9. Comparison of classical Rayleigh number **Ra** and modified Rayleigh number $\mathbf{Ra}_m$ to characterize supercritical natural convection: (a: **Ra** versus $\Delta T_w = T_w - T_{pc}$; b: **Nu** versus **Ra**; c: $\mathbf{Ra}_m$ versus ΔT_w; d: **Nu** versus $\mathbf{Ra}_m$).

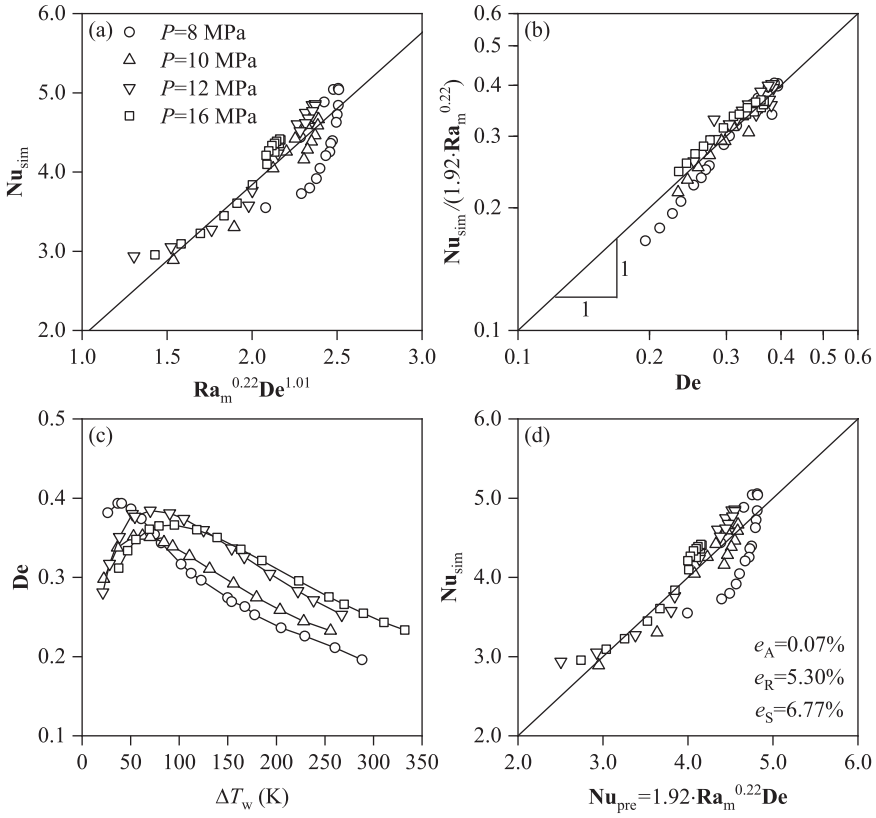


Fig. 10. Correlation and scaling law for supercritical natural convection heat transfer (a: **Nu** versus $\mathbf{Ra}_m^{0.22}\,\mathbf{De}^{1.01}$; b: scaling law of **Nu** ~ **De** c: Effect of ΔT_w on heat transfer deterioration number **De**; d comparison of simulation based on **Nu** with correlation predicted $\mathbf{Nu}_{pre}$.

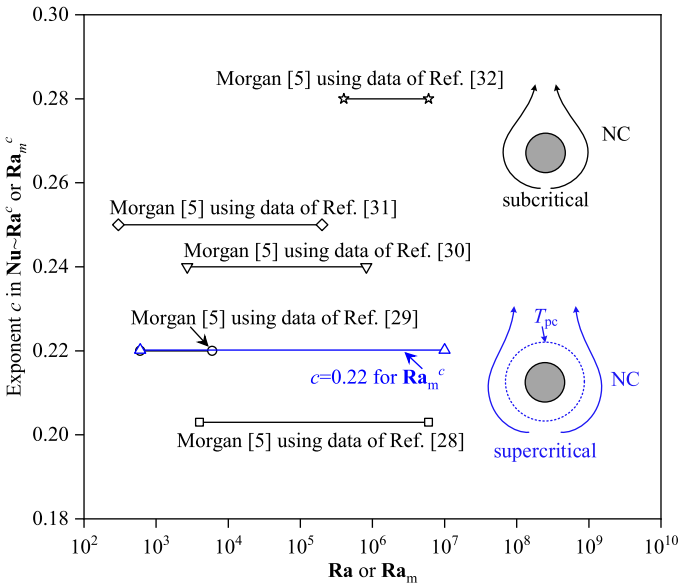


Fig. 11. Comparison of the exponent c in $\mathbf{Nu} \sim \mathbf{Ra}^c$ or $\mathbf{Ra}_m^c$ for supercritical natural convection and those for subcritical natural convection existing in the literature.

present work highlighted the natural convection in the bulk fluid region and vapor-like-layer effect near the wall. The developed scaling law and correlation were valid over wide data ranges. Future work is recommended to extend the scaling law to more working fluids and expanded parameter ranges. The 3D effect with short heater length, inclination angle, and turbulent flow should also be investigated in the future.

4. Conclusions

Some key conclusions from this study can be summarized as follows:

- ✓ Numerical simulations were performed to investigate natural convection heat transfer of supercritical fluids, using a horizontal thin wire as the heater and temperature sensor. Non-uniform cells with local refinement near the heater wire was used to couple the solid heat source and surrounding fluid. The simulation results matched the measured values well.
- ✓ The physical model decoupled the whole flow field into a vapor-like-layer region and bulk fluid region. Thermal conduction is the dominant heat-transfer mechanism in the vapor-like layer, whereas natural convection dominates in the bulk fluid region.
- ✓ The resistance ratio $\boldsymbol{\Theta}$ of the vapor-like-layer was defined in Eq. (16). The equivalent, dimensionless vapor-like-layer sizes were shown to have a self-similarity characteristic with respect to $\boldsymbol{\Theta}$, i.e., the layer size was the same for identical $\boldsymbol{\Theta}$ values, irrespective of the pressure, bulk fluid temperature, and heat flux.
- ✓ A modified Rayleigh number was defined in the bulk fluid region, using $T_{pc} - T_b$ and $0.5(T_{pc} + T_b)$, which were the temperature difference and reference temperature, respectively, to define the physical properties of supercritical fluids, satisfying the fact that the

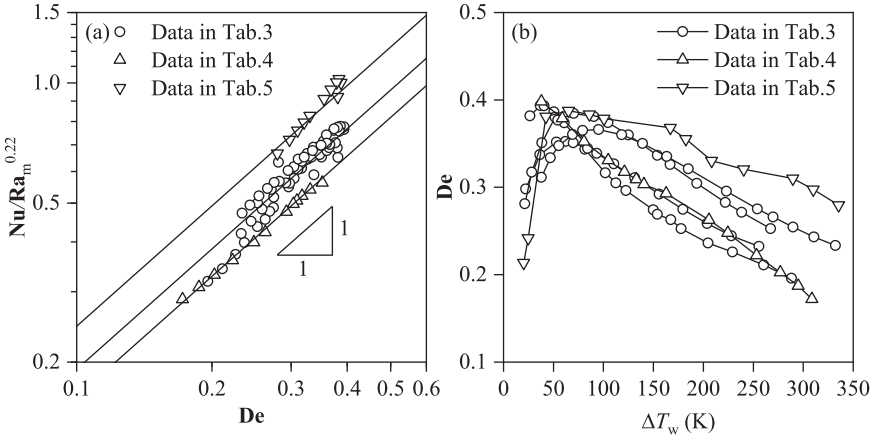


Fig. 12. Scaling law of $\mathbf{Nu} \sim \mathbf{De}$ (a) and effect of ΔT_w on **De** (b), noting that the three sets of data are shown in Tables 3, 4 and 5.

Table 4
Additional simulation results of sCO_2 with T_b= 303.2 K, L= 22.0 mm and D_0 = 140 μm.

No.	P (MPa)	q_w (kW/m^2)	T_w (K)	ΔT_w (K)	**Nu**	$\mathbf{Ra}_m$	$\boldsymbol{\Theta}$	R_S/R_0	**De**
1	11	121.7	360.8	38.0	4.91	23482.4	0.66	1.65	0.40
2	11	154.3	381.6	58.8	5.88	40076.1	0.75	1.98	0.38
3	11	185.9	403.4	80.5	6.36	61582.5	0.80	2.28	0.35
4	11	219.9	427.6	104.7	6.57	85431.6	0.84	2.54	0.33
5	11	242.2	443.8	120.9	6.60	102955.9	0.86	2.71	0.32
6	11	258.7	455.8	133.0	6.59	115936.7	0.87	2.82	0.31
7	11	269.3	463.5	140.6	6.58	125170.9	0.88	2.89	0.30
8	11	299.6	485.6	162.7	6.51	146508.5	0.89	3.05	0.29
9	11	359.1	528.6	205.7	6.31	217244.8	0.91	3.47	0.26
10	11	385.4	547.3	224.5	6.22	264516.8	0.92	3.71	0.25
11	11	425.9	576.2	253.3	6.07	377342.4	0.93	4.18	0.22
12	11	459.9	599.9	277.1	5.95	507712.1	0.93	4.61	0.20
13	11	485.5	617.8	295.0	5.85	651276.5	0.94	5.01	0.19
14	11	505.3	631.5	308.7	5.78	844677.1	0.94	5.46	0.17

Table 5
Simulated sH_2O heat transfer data with T_b= 600.2 K, L= 22.0 mm and D_0 = 70 μm.

No.	P (MPa)	q_w (kW/m^2)	T_w (K)	ΔT_w (K)	**Nu**	$\mathbf{Ra}_m$	**Θ**	R_S/R_0	**De**
1	25	917.4	678.1	20.1	1.84	300.9	0.26	1.21	0.21
2	25	956.7	682.8	24.8	1.84	326.8	0.30	1.24	0.24
3	25	1091.9	701.6	42.5	1.87	427.9	0.42	1.35	0.31
4	25	1224.5	723.1	65.1	2.55	540.5	0.53	1.47	0.36
5	25	1341.4	743.9	85.9	3.85	660.9	0.60	1.57	0.38
6	25	1419.7	758.6	100.6	4.30	751.5	0.63	1.64	0.39
7	25	1752.7	825.1	167.1	4.91	1244.0	0.74	1.94	0.38
8	25	1827.3	840.6	182.5	4.92	1380.1	0.76	2.00	0.38
9	25	1952.4	866.4	208.4	4.91	1646.8	0.78	2.13	0.37
10	25	2107.5	898.5	240.5	4.85	2001.1	0.81	2.27	0.36
11	25	2345.8	947.7	289.7	4.73	2748.2	0.83	2.52	0.33
12	25	2445.8	968.1	310.1	4.67	3108.7	0.84	2.63	0.32
13	25	2571.4	993.5	335.4	4.59	3565.2	0.85	2.75	0.31
14	25	2700.4	1019.3	361.2	4.53	4191.7	0.86	2.90	0.30
15	25	2912.0	1060.9	402.9	4.41	5300.2	0.88	3.14	0.28

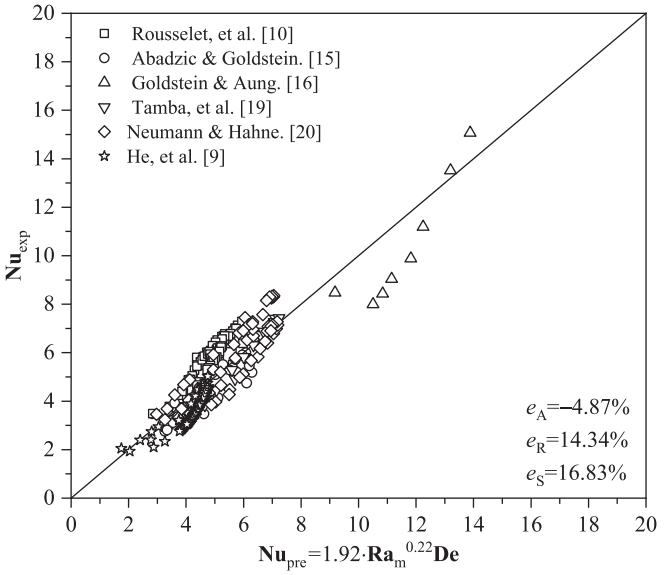


Fig. 13. Comparison of the measured Nusselt number in the literature and the present correlation of **Nu**.

natural convection intensity would be enhanced with increasing wall temperature.

✓ The heat transfer deterioration number **De** was introduced, for the first time, to comprehensively integrate the vapor-like-layer's resistance ratio and size. **Nu** was successfully correlated as $\boldsymbol{Nu} = 1.92\cdot\boldsymbol{Ra}_m^{0.22}\boldsymbol{De}$, indicating the linear scaling law of **Nu**~**De**. The exponent of 0.22 for $\mathbf{Ra}_m$ was in the range of that for natural convection without phase change at subcritical pressures.

✓ The scaling laws and correlation based on 63 sets of numerical simulation and experimental data were found to be suitable for other fluids, such as supercritical water and the operating parameters of supercritical CO_2, even though these data were not involved in the development of the correlation.

CRediT authorship contribution statement

Guanglin Liu: Validation, Project administration. **Yulin Mao:** Visualization, Software, Investigation. **Jinliang Xu:** Writing – review & editing, Supervision, Funding acquisition, Formal analysis, Conceptualization. **Yaqin Liu:** Writing – original draft, Methodology, Formal analysis, Data curation.

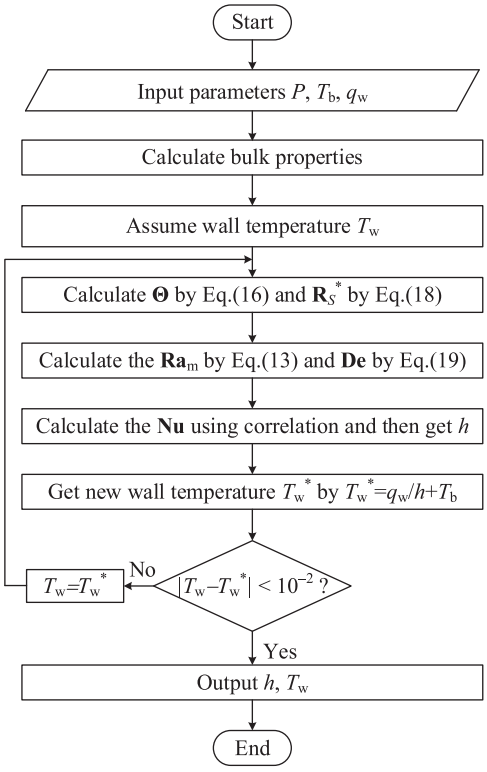


Fig. 14. Calculation procedure for **Nu** and T_w using the proposed correlation for supercritical natural convection.

Declaration of Competing Interest

The authors declare that they have no known competing financial interests or personal relationships that could have appeared to influence the work reported in this paper.

Acknowledgements

This work was supported by the National Natural Science Foundation of China (No. 52130608).

References

[1] T.L. Bergman, A.S. Lavine, F.P. Incropera, D.P. DeWitt. Fundamentals of Heat and Mass Transfer, 7th ed..,, John Wiley & Sons,, Hoboken, NJ, 2011.

[2] S. Kakac, W. Aung, R. Viskanta (Eds.), Natural Convection: Fundamentals and Applications, Hemisphere Publishing Corporation, Washington, 1985.
[3] N. LeFrancois, V. Lamenta, J. Nedic, M. Tetreault-Friend, Flow visualization and heat transfer measurements of molten salt natural convection, Int. J. Heat. Mass. Transf. 253 (2025) 127392.
[4] S. Hansda, S. Soren, A.K. Hussein, A. Chattopadhyay, M.M. Molla, Z.T. Al-Sharify, M.S. Alhassan, M.B.Ben Hamida, B. Souayeh, Natural convection in U-shaped cavities with nanofluids: A comprehensive review of heat transfer mechanisms and applications, Int. Commun. Heat. Mass. Transf. 172 (2026) 110157.
[5] V.T. Morgan, The Overall Convective Heat Transfer from Smooth Circular Cylinders, Adv. Heat. Transf. 11 (1975) 199–264.
[6] S.K.S. Boetcher, Natural Convection from Circular Cylinders, Springer,, Cham, Heidelberg, New York, Dordrecht, London, 2014.
[7] S.Özgür Atayılmaz, İ. Teke, Experimental and numerical study of the natural convection from a heated horizontal cylinder, Int. Commun. Heat. Mass. Transf. 36 (2009) 731–738.
[8] Q.Y. Wang, J.L. Xu, C.R. Zhang, B.T. Hao, L.Y. Cheng, A Critical Review on Heat Transfer of Supercritical Fluids, Heat. Transf. Eng. 44 (2023) 1969–1994.
[9] X.T. He, J.L. Xu, X.J. Yu, J. Xie, Distinguishing evaporation-like and boiling-like modes of pseudo-boiling in supercritical pressures, Int. J. Heat. Mass. Transf. 214 (2023) 124417.
[10] Y. Rousselet, G.R. Warrier, V.K. Dhir, Natural Convection From Horizontal Cylinders at Near-Critical Pressures—Part I: Experimental Study, J. Heat. Transf. 135 (2013) 022501.
[11] G.R. Warrier, Y. Rousselet, V.K. Dhir, Natural Convection From Horizontal Cylinders at Near-Critical Pressures—Part II: Numerical Simulations, J. Heat. Transf. 135 (2013) 022502.
[12] C.S. Yan, Y. Zhang, X.Y. Zhang, W.X. Wang, B. Zhao, Numerical study on natural convection heat transfer of supercritical CO_2 in an infinite space, Int. Commun. Heat. Mass. Transf. 156 (2024) 107680.
[13] B.G. Zhu, J.L. Xu, X.M. Wu, J. Xie, M.J. Li, Supercritical “boiling” number, a new parameter to distinguish two regimes of carbon dioxide heat transfer in tubes, Int. J. Therm. Sci. 136 (2019) 254–266.
[14] B.G. Zhu, J.L. Xu, C.S. Yan, J. Xie, The general supercritical heat transfer correlation for vertical up-flow tubes: K number correlation, Int. J. Heat. Mass. Transf. 148 (2020) 119080.
[15] E. Abadzic, R.J. Goldstein, Film Boiling and Free Convection Heat Transfer to Carbon Dioxide Near the Critical State, Int. J. Heat. Mass. Transf. 13 (1970) 1163–1175.
[16] R.J. Goldstein, W. Aung, Heat Transfer by Free Convection From a Horizontal Wire to Carbon Dioxide in the Critical Region, J. Heat. Transf. 90 (1968) 51–55.
[17] E. Hahne, R. Neumann, Boiling-like Phenomena in Free-Convection Heat Transfer at Supercritical Pressures, Wärme- und Stoffübertrag. 15 (1981) 171–180.
[18] K.K. Knapp, R.H. Sabersky, Free Convection Heat Transfer to Carbon Dioxide Near the Critical Point, Int. J. Heat. Mass. Transf. 9 (1966) 41–51.
[19] J. Tamba, T. Takahashi, T. Ohara, T. Aihara, Transition from boiling to free convection in supercritical fluid, Exp. Therm. Fluid. Sci. 17 (1998) 248–255.
[20] R.J. Neumann, E.W.P. Hahne, Free Convective Heat Transfer to Supercritical Carbon Dioxide, Int. J. Heat. Mass. Transf. 23 (1980) 1643–1652.
[21] K. Nishikawa, T. Ito, H. Yamashita, Free-Convective Heat Transfer to a Supercritical Fluid, J. Heat. Transf. 95 (1973) 187–191.
[22] B. Zhang, J.L. Xu, X.J. Yu, J. Xie, G.L. Liu, Quantitative measurement of pseudo-vapor-layer thickness and its contribution on supercritical heat transfer, J. Supercrit. Fluids 237 (2026) 107055.
[23] J.P. Holman, Experimental Methods for Engineers, McGraw-Hill,, York, 2012.
[24] F.H. Champagne, C.A. Sleicher, O.H. Wehrmann, Turbulence measurements with inclined hot-wires Part 1. Heat transfer experiments with inclined hot-wire, J. Fluid. Mech. 28 (1967) 153–175.
[25] NIST, NIST Reference Fluid Thermodynamic and Transport Properties, National Institute of Standards and Technology, Gaithersburg, MD, USA.
[26] S.W. Churchill, H.H.S. Chu, Correlating equations for laminar and turbulent free convection from a horizontal cylinder, Int. J. Heat. Mass. Transf. 18 (1975) 1049–1053.
[27] M. Koecher, A. Krieg, Ebene Geometrie, Springer-Verlag,, 2013, p. 116.
[28] C.W. Rice, Free and forced convection of heat in gases and liquids, Trans. Am. Inst. Electr. Eng. XLII (1923) 653–706.
[29] R. Lemlich, Effect of vibration on natural convective heat transfer, Ind. Eng. Chem. 47 (1955) 1070–1074.
[30] O. Schurig, C. Frick, Heat and current-carrying capacity of bare conductors for outdoor service, Gen. Electr. Rev. 33 (1930) 141–157.
[31] J. Petavel, On the heat dissipated by a platinum surface at high temperatures. Part IV. Thermal emissivity in high-pressure gases, Philos. Trans. R. Soc. A 197 (1901) 229–254.
[32] W. Koch, Über die wärmeabgabe geheizter rohre bei verschiedener neigung der rohrachse, Gesundh. Ing. Beih. 1 (1927) 1–29.